Incorporating Chaotropic/Kosmotropic Chemistries onto Plasmonic Nanoheater to Boost Steam Generation Beyond its Photothermal Property

Carice Chong[‡], *Zher Nin Tan*[‡], *Siew Kheng Boong, Zhi Zhong Ang, Shi Xuan Leong, Yih Hong Lee, Haitao Li, Hiang Kwee Lee**

C. Chong, Z. N. Tan, S. K. Boong, Z. Z. Ang, S. X. Leong, Y. H. Lee, Prof. H. K. Lee
Division of Chemistry and Biological Chemistry, School of Chemistry, Chemical Engineering and Biotechnology
Nanyang Technological University
21 Nanyang Link, Singapore 637371.
E-mail: hiangkwee@ntu.edu.sg

H. Li
School of Chemistry and Chemical Engineering
Yangzhou University
Yangzhou, 225002, PR China.

Prof. H. K. Lee
Institute of Materials Research and Engineering
The Agency for Science, Technology and Research (A∗STAR)
2 Fusionopolis Way, #08-03, Innovis, 138634, Singapore.

Prof. H.K. Lee
Centre for Hydrogen Innovations
National University of Singapore (Singapore)
E8, 1 Engineering Drive 3, Singapore 117580

[‡]These authors contributed equally to this work.

Keywords: chaotropic, kosmotropic, steam generation, photothermal, thermoplasmonic

Abstract

Photothermal steam generation promises decentralized water purification, but current methods suffer from slow water evaporation even at high photothermal efficiency of ~98 %. This drawback arises from the high latent heat of vaporization that is required to overcome the strong and extensive hydrogen bonding network in water for steam generation. Here, we boost light-to-vapor conversion by incorporating chaotropic/kosmotropic chemistries onto plasmonic nanoheater to manipulate water intermolecular network at the point-of-heating. Our chaotropic-plasmonic nanoheater affords rapid light-to-vapor conversion (2.79 kg m^{-2} h^{-1} kW^{-1}) at ~83 % efficiency, with the steam generation rate up to 6-fold better than kosmotropic platforms or emerging photothermal designs. Notably, the chaotropic-plasmonic nanoheater also lowers the enthalpy of water vaporization by 1.6-fold when compared to bulk water, signifying that a correspondingly higher amount of steam can be generated with the same energy input. Simulation studies unveil chaotropic surface chemistry is crucial to disrupt water hydrogen bonding network and suppress the energy barrier for water evaporation. Using the chaotropic-plasmonic nanoheater, we purify organic-polluted water at ~100 % efficiency, a feat otherwise challenging in conventional treatments. Our work offers a unique chemistry approach to boost light-driven steam generation beyond a material photothermal property.

1. Introduction

Photothermal steam generation is an emerging water purification strategy to tackle the global water crisis facing the sustainable development of human civilizations, whereby over 2 billion people worldwide is still deprived of safe potable water.[1] Compared to various chemical and physical (e.g., reverse osmosis) treatment methods, photothermal steam generation provides unique advantage arising from its ability to transform light energy into heat to promote water evaporation for subsequent collection as clean water.[2-4] This evaporation-and-condensation approach enables the efficient and simultaneous removal of diverse inorganic, organic, and biological contaminants to generate clean water.[5-7] The benefits offered by photothermal steam generation thus circumvent the limitations of modern water treatment approaches, whereby the latter requires (1) multi-step processes to treat different contaminants and (2) cumbersome post-treatment removal of chemical additives.[8, 9] Together with the use of abundant (sun)light and/or green electricity to power energy-efficient lamps, photothermal steam generation promises distributed, on-site water purification by alleviating the traditional need for centralized treatment facilities and/or trained personnel.[10, 11]

The recent advent of photothermal steam generation notably drives the development of plasmonic,[12] polymeric,[13, 14] and carbon-based materials[15, 16] with efficient light absorption and conversion properties. Current photothermal designs to accelerate water evaporation generally focus on improving heat generation via (1) materials engineering and/or (2) the formation of hybrid materials.[17-19] For instance, the shape and size of plasmonic nanomaterials can be controlled to tailor their optical properties towards broadband light absorption or improving wavelength-specific absorption.[18] These enhanced light-matter interactions create high-energy plasmons for heat generation upon their non-radiative decay, a phenomenon known as the thermoplasmonic effect.[20] Moreover, hybrid photothermal ensemble fabricated by coating graphene with a layer of metal-organic framework (MOF) has also been demonstrated to achieve efficient photothermal conversion (~98 %) via the localization of heat at the graphene-MOF interface.[17] Despite having high photothermal conversion at near 100 % efficiency, photothermal steam generation still suffers low evaporation rates of <2 kg m^{-2} h^{-1} kW^{-1} which hinders real-world application. This formidable drawback arises from the high latent heat of vaporization that is required to overcome the strong and extensive hydrogen bonding network in water for steam generation.[21] It is thus necessary to devise new strategy beyond a material's intrinsic photothermal property to boost light-mediated water evaporation towards practical water purification applications.

Herein, we achieve rapid steam generation and efficient water purification by designing functional, molecular monolayers on photothermal material surfaces to manipulate the water hydrogen bonding network and facilitate corresponding evaporation process. Our strategy integrates two key concepts to boost light-to-vapor transformation. (1) A model thermoplasmonic platform comprising of nanoporous gold bowl (NPGB) for efficient heat generation. NPGB also possesses large specific surface area to maximize its interaction with water molecules and facilitate heat transfer. (2) The use of chaotropic/kosmotropic molecular monolayers to interact and weaken/strengthen water hydrogen bonding network at the point-of-heating. Chaotropic molecules will disrupt/weaken hydrogen bonds between water molecules to promote water evaporation, whereas kosmotropic molecules reinforce/strengthen water-water interactions to retard steam generation.[22] Our novelty thus lies in the use of surface chemistries for the unprecedented control over water hydrogen bonding network to suppress the energy barrier for water vaporization. This approach is notably distinct from conventional hydrophilic modification of photothermal platform that instead aims to facilitate water uptake and transfer.

Systematic investigation across eight different surface chemistries on the plasmonic nanoheater evidently showcases a boost in photothermal steam generation from 2.35 kg m^{-2} h^{-1} kW^{-1} to 2.79 kg m^{-2} h^{-1} kW^{-1} as the monolayer transits from a kosmotropic to a chaotropic character, respectively. Using our best-performing chaotropic-plasmonic nanoheater, we achieve superior steam generation rate up to 6-fold faster than emerging photothermal materials and a notable light-to-vapor conversion efficiency of ~83 %. Extensive corroboration of experimental and simulation investigations unravels that the chaotropic molecular monolayer is important to destabilize water hydrogen bonding network directly on the photothermal surface, thereby reducing the apparent energy demand for water evaporation. As a proof-of-concept application, we further employ our chaotropic-plasmonic nanoheater to treat organic-polluted water at a purification efficiency of ~99.99 %, which is >6-fold better than traditional chemical method involving Fenton reaction. Our unique chaotropic/kosmotropic designs to manipulate water hydrogen bonding network thus offer valuable insights to chemically boost steam generation beyond a material's photothermal ability. We envision the parallel advancements in (1) functional surface chemistry and (2) efficient photothermal materials are critical to expedite progress towards decentralized (sea)water purification technologies for combating the global water crisis.

2. Results and Discussion

The incorporation of chaotropic/kosmotropic molecular monolayer onto thermoplasmonic nanoporous gold bowl (NPGB) plays a central role to manipulate water hydrogen bonding network directly at the point-of-heating for enhanced steam generation (Figure 1A). We first synthesize the NPGBs using our reported two-step method involving the initial growth of NPGBs onto AgCl nanocube sacrificial templates, followed by the chemical removal of the AgCl.[18] As-synthesized NPGBs exhibit a hemispherical bowl-like structure (diameter, 462 ± 35 nm) with uniformly interconnected ligaments (thickness, ~17 nm; Figure 1B; Figure S1).[18] We then fabricate the thermoplasmonic platform by depositing NPGB nanoparticles (20 – 100 mg cm^{-2}) onto a polyvinylidene difluoride membrane (PVDF; pore size, 220 nm). The PVDF membrane serves as a porous, floating support to position the photothermal layer at the gas-liquid interface for interfacial heating while facilitating the transfer of bulk water to the NPGB layer.[23] The NPGBs are mainly deposited on one side of PVDF surface to form a black NPGB/PVDF thin film (diameter, 1 cm; Figure 1B; Figure S2) because the NPGBs are bigger than the PVDF pores. Diffuse reflectance spectroscopy (DRS) measurement of NPGB/PVDF film attributes its dark appearance to the broadband light absorption in the visible-NIR regions (i.e., 450 nm – 1000 nm; Figure S3) arising from the extensive plasmonic couplings within the NPGB layer.

To obtain the as-designed chaotropic/kosmotropic platforms, we chemisorb a self-assembled monolayer of thiolated molecules onto NPGB surfaces via the formation of strong Au-S bonds. We select eight different para-substituted aromatic thiols (Figure 1C; Figure S4) for fair evaluations on the effects of various surface chemistries on the water hydrogen bonding network. These thiols include 4-methoxybenzenethiol (MethoxyBT), 4-mercaptobenzoic acid (MBA), 4-fluorothiophenol (FTP), 4-mercaptophenol (MP), benzenethiol (BT), 4-methylbenzenethiol (MethylBT), 4-mercaptophenylboronic acid (MPBA), and 4-bromothiophenol (BTP). These model thiols are chosen because they can interact differently with water molecules via various intermolecular interactions, such as hydrogen bonding and dipole interactions, as well as different types/numbers of donor/acceptor atoms. We affirm the successful chemical modifications of NPGB surfaces through the emergence of characteristic Au 4f and S 2p X-ray photoelectron spectroscopy (XPS) peaks of Au-S bond (Figure S5),[24] thereby indicating that the para-substituents are indeed oriented outwards to interact with adjacent water molecules. Moreover, the surface hydrophilicity of all platforms is similar

(contact angle, 51 – 82°) which excludes the effect of material wettability on photothermal steam generation (Figure S6).

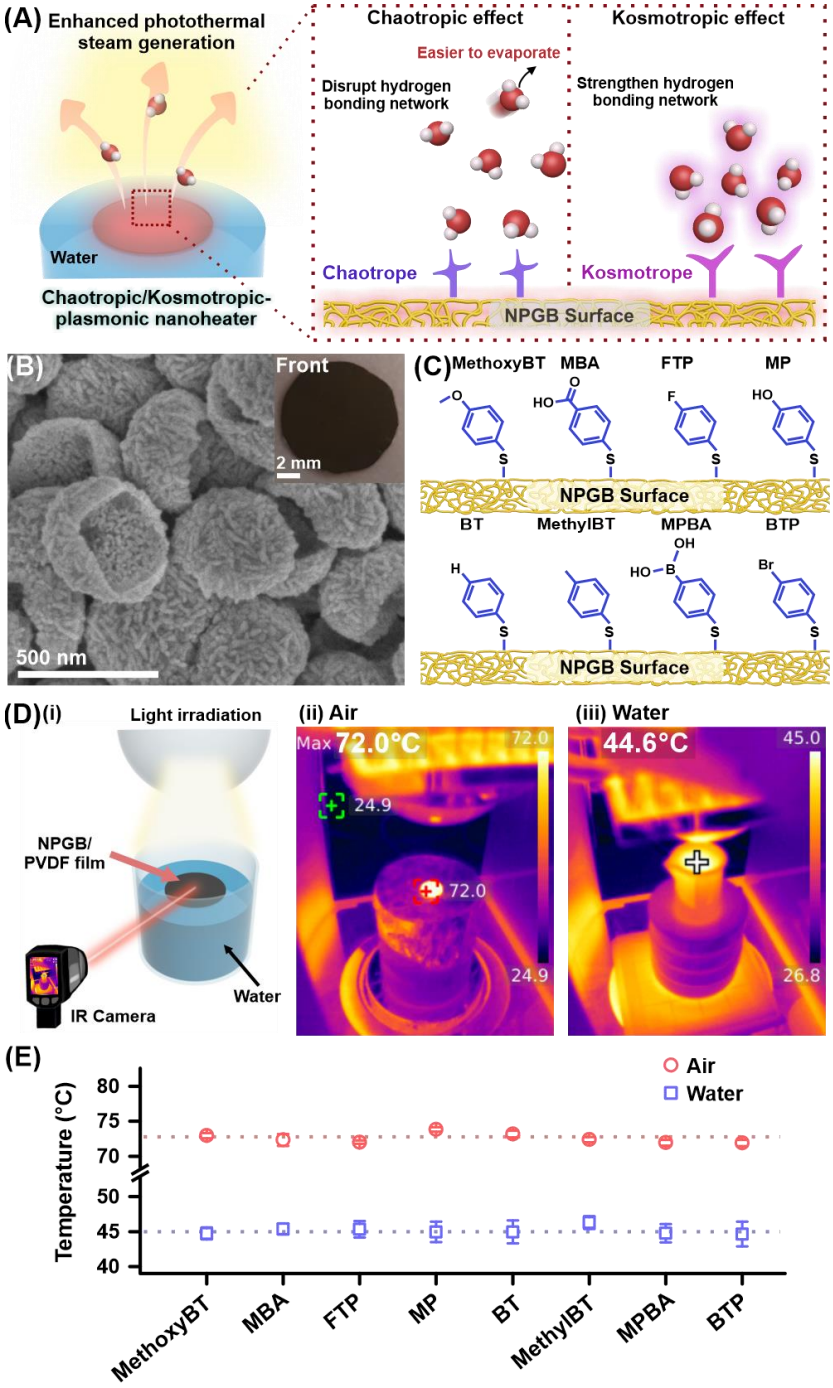

Figure 1. Chaotropic/kosmotropic plasmonic nanoheaters for photothermal steam generation. (A) Scheme illustrating the use of chaotropic/kosmotropic-plasmonic nanoheater to tune and boost photothermal steam generation. (B) Scanning electron microscope (SEM) image of as-synthesized NPGB. Inset, front-view digital image of NPGB/PVDF membrane. (C) Molecular structure of various para-substituted thiolated arenes used for NPGB surface functionalizations. (D)(i) Photothermal setup to monitor NPGB/PVDF surface temperature

upon light irradiation. Thermograms of NPGB/PVDF film (ii) in air and (iii) on water surface upon light irradiation. (E) Photothermal temperature of the eight surface-functionalized NPGB/PVDF platforms when placed in air or on water surface upon light irradiation.

Notably, there are two important components in our design to realize efficient photothermal steam generation, namely (1) a hot photothermal layer to evaporate water and (2) the incorporation of functional surface chemistries to manipulate water-water interactions. We first evaluate the localized photothermal heating of NPGB/PVDF platform (mass loading of as-synthesized NPGB, 69 mg cm^{-2}) by tracking its surface temperature using an infrared (IR) camera (Figure 1D-i). In a typical evaporation set-up, we place the NPGB/PVDF platform on water surface and monitor the water loss in real time using an analytical balance during light irradiation. The light irradiance is clearly uniform across the entire NPGB/PVDF film (<4 % deviation; Figure S7) to allow accurate evaluation on subsequent steam generation performances. When placed in air, the surface temperature of NPGB/PVDF platform rapidly increases from ~25 ^{o}C to ~72 ^{o}C upon light irradiation (Figure 1D-ii), achieving a thermoplasmonic conversion efficiency of ~75% (Supporting Information 1). When placed on water surface, NPGB/PVDF platform attains a lower equilibrium surface temperature of ~45 ^{o}C, signifying the effective transfer of thermal energy from the NPGB layer to the underlying water during interfacial photothermal heating (Figure 1D-iii). The photothermal heating of NPGB/PVDF platform is stable for over 3 hours (Figure S8) and can be instantaneously and reproducibly triggered across ten irradiation cycles (Figure S9). More importantly, all surface-modified NPGB/PVDF platforms attain consistent photothermal temperatures in both air and water (<1 % deviation) under identical light irradiation. These results clearly underscore the negligible effect of molecular monolayer on NPGB's intrinsic thermoplasmonic property (Figure 1E), a key criterion to effectively isolate the contributions of chaotropicity/kosmotropicity on photothermal steam generation. Hereon, we will name the NPGB/PVDF platform as plasmonic nanoheater due to its on-demand heating upon light irradiation.

We subsequently optimize the plasmonic nanoheater for photothermal steam generation by tuning the (1) thermoplasmonic material and (2) NPGB mass loading (Figure 2A). Using MethoxyBT as a model, we note two major findings for plasmonic nanoheater optimization. (1) MethoxyBT-modified NPGB generates steam at a rate of ~2.79 kg m^{-2} h^{-1} kW^{-1}, which is >1.1-fold and 3.3-fold faster than MethoxyBT-modified solid gold bowl and neat PVDF membrane,

respectively, under identical irradiation power (Figure S10). Notably, the superior photothermal steam generation of NPGB over solid gold bowl, albeit their similar photothermal responses, exemplifies the importance of large specific surface area to facilitate heat transfer to and interaction with water (Figure S10). (2) As NPGB mass loading increases from 20 to 100 mg cm^{-2}, water evaporation rate and photothermal temperature initially increase and eventually plateau beyond a mass loading of 69 mg cm^{-2} (Figure S11). The optimal mass loading at 69 mg cm^{-2} is due to the limited light penetrability into a thick NPGB particle layer, as evident from the comparison of x-z surface-enhanced Raman spectroscopy (SERS) intensity-distance profile with the cross-sectional SEM image of the plasmonic nanoheater (Figure S12). It is noteworthy that the full-width-at-half-maximum (FWHM) is related to the penetrability of light into a thick particle layer,[25] whereby a larger FWHM value indicates deeper light penetration and vice versa. We observe FWHM gradually increases from ~14 μm to ~15.5 μm when we increase mass loading from 23 mg cm^{-2} to 69 mg cm^{-2}. Further increase of mass loading beyond 69 mg cm^{-2} leads to a plateau in the FWHM recorded from the x-z SERS image. Moreover, the water evaporation rate can also be precisely modulated by controlling the light irradiance in an indoor setting using energy-efficient LED lamps (Figure S13A-C). Achieving indoor water evaporation could be beneficial to collect treated water in a sanitary environment, thereby creating enormous opportunities for indoor applications such as urban farming and continuous water treatment. More importantly, the power-normalized water evaporation rates are similar (<4 % deviation) even when light irradiance is increased by ~2-fold. This is concrete evidence that the power-normalized evaporation rate used in our study is independent on the absolute light irradiance, thereby providing a useful benchmark to compare our design with other photothermal platforms (e.g., commonly at 1 kW m^{-2}). Collectively, we thus optimize the plasmonic nanoheater using NPGB and at a mass loading of 69 mg cm^{-2} for subsequent experiments, as justified by its efficient light absorption and photothermal conversion.

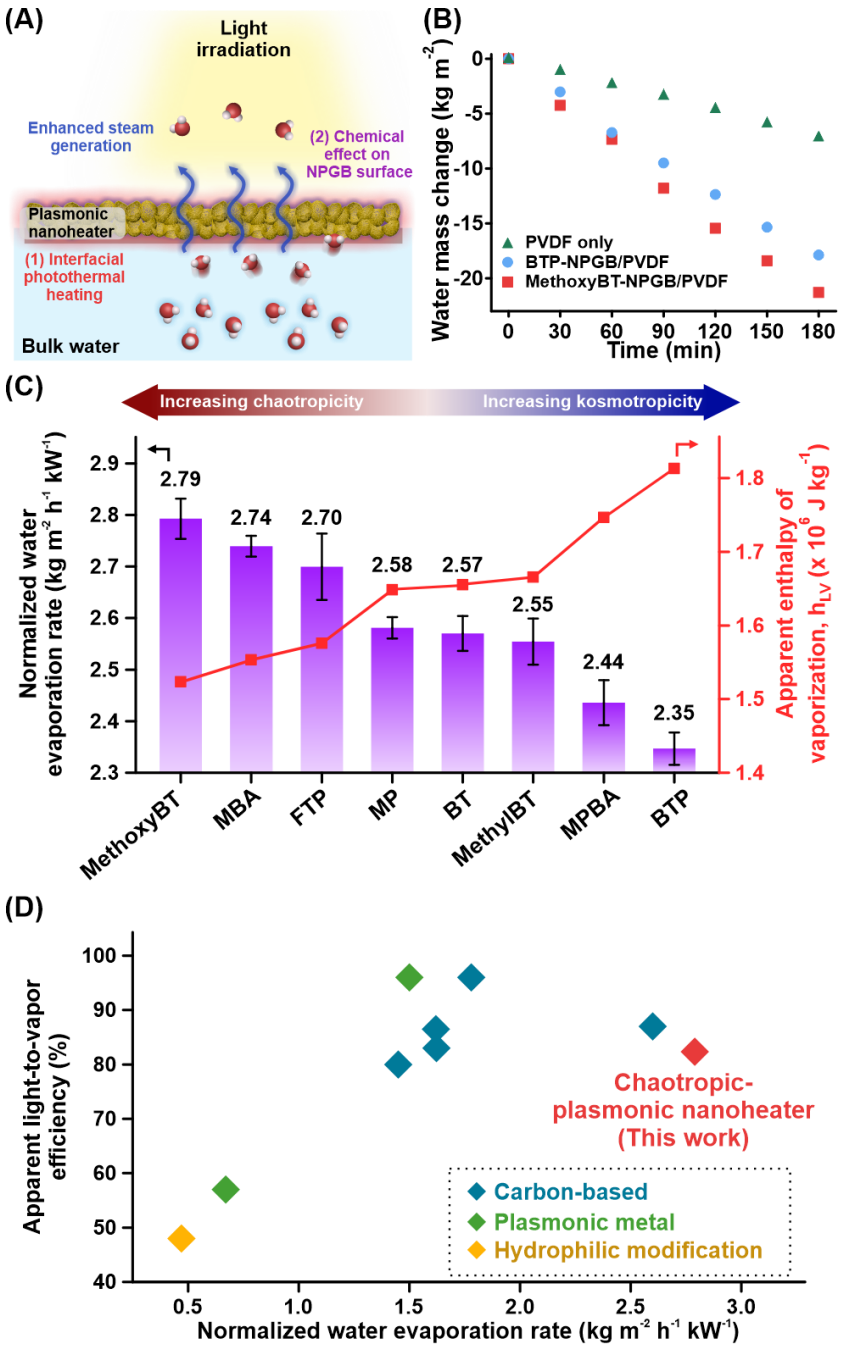

Figure 2. Photothermal steam generation performances of various plasmonic nanoheaters. (A) Scheme depicting the importance of efficient photothermal conversion and the use of chaotropic/kosmotropic surface chemistries to boost steam generation. (B) Time-dependent changes to water mass when subjected to photothermal steam generation using MethoxyBT- and BTP-plasmonic nanoheaters (NPGB/PVDF platform). Neat PVDF platform is included for comparison. (C) Photothermal water evaporation rate and apparent enthalpy of vaporization of the eight types of surface-functionalized plasmonic nanoheater. (D) Comparison of the photothermal steam generation performances of our chaotropic-plasmonic design with previously reported photothermal platforms.[11, 17, 26-31]

Having established an optimized plasmonic nanoheater, we further investigate the effects of the chaotropic/kosmotropic chemistries on photothermal steam generation. All surface-modified plasmonic nanoheaters generally lead to consistent and linear loss of water mass over a long duration of 3 h under light irradiation. By quantifying the gradient of respective mass change-time plots, we observe that MethoxyBT-plasmonic nanoheater attains fastest water evaporation at ~2.79 kg m^{-2} h^{-1} kW^{-1}. This is followed by MBA-, FTP-, MP-, BT-, MethylBT-, MPBA-, and BTP-plasmonic nanoheaters with a decreasing water evaporation rate of ~2.74, 2.70, 2.58, 2.57, 2.55, 2.44, and 2.35 kg m^{-2} h^{-1} kW^{-1} (Figure 2C), respectively. Further comparison of MethoxyBT- and BTP-plasmonic nanoheaters also reveals a 17 % boost to water evaporation rate simply by programming the surface chemistry on the thermoplasmonic material. We observe that both MethoxyBT- and BTP-plasmonic nanoheaters demonstrate excellent stability/durability, as evident from the consistent steam generation rates (<7 % deviation) upon light irradiation over nine successive test cycles. This finding provides direct evidence that our plasmonic nanoheater is robust and able to maintain its photothermal steam generation performances over extended usage (Figure S14). The MethoxyBT design also enables faster photothermal steam generation than the MPBA counterpart even though the latter is more hydrophilic.

More importantly, the apparent enthalpy of vaporization (h_{LV}) of the eight types of surface-functionalized plasmonic nanoheater can be estimated by[32]

$$h_{LV\ (\text{plasmonic nanoheater})} = \frac{R_{\text{bulk water}}}{R_{\text{plasmonic nanoheater}}} \times h_{LV\ (\text{bulk water})} \qquad (1)$$

where $h_{LV\ (\text{plasmonic nanoheaater})}$ is the enthalpy of vaporization of the plasmonic nanoheater, $R_{\text{bulk water}}$ and $R_{\text{plasmonic nanoheater}}$ are the water evaporation rates of bulk water and plasmonic nanoheater, respectively, and $h_{LV\ (\text{bulk water})}$ is the enthalpy of vaporization of bulk water. As the enthalpy of vaporization decreases when the temperature increases, the bulk water evaporation was performed at 45 ^{o}C (i.e., at the photothermal temperature of the plasmonic nanoheaters) to accurately identify the vaporization enthalpy under actual photothermal conditions for fair comparison. We observe an opposite trend between the calculated h_{LV} values and the water evaporation rate of various surface molecules. For instance, MethoxyBT has the lowest h_{LV} of ~1.52×10^6 J Kg^{-1} and afford the fastest steam generation rate of 2.79 kg m^{-2} h^{-1} kW^{-1}, whereas BTP has the highest h_{LV} value of ~1.81×10^6 J Kg^{-1} but slowest water vaporization of 2.35 kg m^{-2} h^{-1} kW^{-1} (Figure 2C). It is also noteworthy that our chaotropic-plasmonic nanoheater

exhibits a ~1.6-fold lower h_{LV} value than the bulk water at 45 °C (h_{LV}, 2.39×10^6 J Kg^{-1}), indicating that a correspondingly higher amount of steam can be generated even with same energy input.

Moreover, our best-performing MethoxyBT-plasmonic nanoheater also provides the highest apparent light-to-vapor conversion efficiency of ~83 % (Figure S15; Supporting Information 2) and an approximately eight percentage points more efficient utilization of light energy for steam generation relative to the BTP design. We attribute its superior light-to-vapor conversion efficiency to the disruption of water hydrogen bonding network by the chaotropic monolayer, whereby this chemical phenomenon reduces the energy barrier for liquid-to-gas transition when compared to the latent heat of bulk water vaporization (to be discussed in next paragraph). It is also noteworthy that our chaotropic-plasmonic nanoheater affords a water evaporation rate up to 6-fold higher than emerging plasmonic/carbon-based materials with better photothermal and/or wetting properties (Figure 2D).[11, 17, 26-31] SERS characterization of the plasmonic nanoheater affirms that the molecular monolayers are chemically robust even after nine cycles of photothermal steam generation (Figure S16). Our results evidently demonstrate that the molecular surface monolayer indeed plays a vital role to chemically drive photothermal steam generation rather than just facilitating water uptake/transfer in conventional hydrophilic surface modification.

We subsequently employ density functional theory (DFT) simulations to unravel the molecular origin behind the superior photothermal steam generation in our chaotropic-plasmonic design. We investigate two key parameters to provide vital insights on the water hydrogen bonding network and the evaporation process, namely the entropy (S) of the free water system and the change in Gibbs free energy of water evaporation ($\Delta G_{evaporation}$; Figure 3A; Supporting Information 3), respectively. On the one hand, the simulated entropy quantifies the disorderness/randomness of the free water system arising from the thiol-water interaction, an important parameter to identify potential chaotropic/komsotropic effects. For instance, a chaotropic molecule is expected to increase the entropy of free water system because it interacts with water molecule(s) to disrupt the hydrogen bonding network and increase the randomness of the water network. On the other hand, $\Delta G_{evaporation}$ determines the spontaneity for one water molecule to escape from the liquid phase into gas phase during water evaporation. That is, a smaller $\Delta G_{evaporation}$ value denotes a lower energy barrier for liquid-to-gas transition. The $\Delta G_{evaporation}$ is notably influenced by the entropy of free water system, whereby a higher

randomness in the water network (e.g. in the case of chaotropic molecule) inhibits the formation of extensive hydrogen bonding between water molecules. Consequently, lesser energy (e.g. $\Delta G_{evaporation}$) is required to overcome the water-water intermolecular interactions for efficient liquid-to-gas transition. Our simulation model comprises of a chaotrope/kosmotrope bonded to a gold cluster with its para-substituent interacting with a network of five water molecules. We first study model thiols with multi-atoms para-substituent to facilitate comparisons and elucidate vital chemical insights.

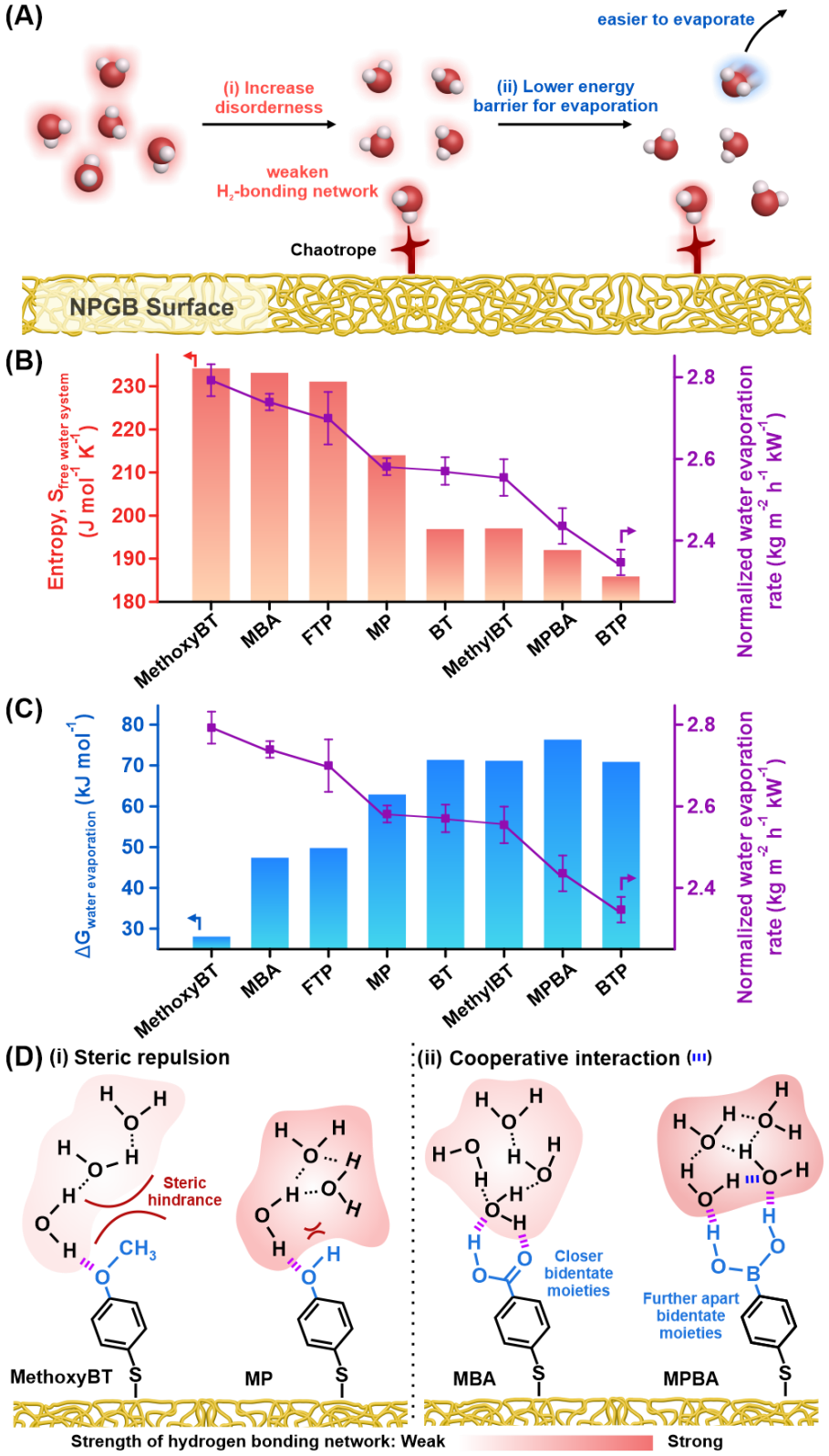

Figure 3. Simulation investigations on the interactions between various surface-modified plasmonic nanoheaters and water intermolecular network. (A) Scheme depicting the importance of chaotropic surface chemistry to (i) disrupt water hydrogen bonding network and (ii) its corresponding enhancement to water evaporation. DFT-simulated (B) entropy (S) and (C) change in Gibbs free energy (ΔG) of various chaotropic/kosmotropic chemistries and their

correlations to experimental water evaporation rate. (D) Schemes depicting the effects of (i) steric repulsion and (ii) cooperative intermolecular interactions of bidentate moieties on the water hydrogen bonding network.

Notably, systematic investigation into the system thermodynamics reveals three general findings. First, the trend of simulated entropy values is directly proportional and well-aligned to the photothermal steam generation performances of respective surface-modified plasmonic nanoheaters. For instance, MethoxyBT-plasmonic nanoheater exhibits the highest entropy of ~234 J mol^{-1} K^{-1} and fastest water evaporation rate of 2.79 kg m^{-2} h^{-1} kW^{-1} (Figure 3B), whereas BTP shows the lowest entropy of ~186 J mol^{-1} K^{-1} and slowest water evaporation rate of 2.35 kg m^{-2} h^{-1} kW^{-1}. Second, the $\Delta G_{evaporation}$ values of all surface chemistries are positive, indicating that liquid-to-gas transition is non-spontaneous and photothermal heat is required to drive water evaporation (Figure 3C). Third, there is an opposite trend between the $\Delta G_{evaporation}$ value and the water evaporation rate of various thiols, whereby MethoxyBT has the lowest $\Delta G_{evaporation}$ of ~28 kJ mol^{-1} while MPBA has the highest value of ~80 kJ mol^{-1}. Our results jointly demonstrate MethoxyBT as a superior chaotrope capable of disrupting water-water interactions to afford a disordered water network (e.g., higher S), whereby water molecules are not optimally positioned/oriented for extensive intermolecular hydrogen bonding. The decrease in intermolecular interactions consequently destabilizes the water network (i.e., elevates free energy of water) and leads to a decrease in the energy barrier for liquid-to-gas transition, as evident from the lowest $\Delta G_{evaporation}$ of MethoxyBT. Conversely, the presence of a more kosmotropic agent (e.g., MPBA) reinforces water-water interactions into an organized water system (e.g., lower S) that is more stable due to the extensive hydrogen bonding present. As a result, the kosmotrope increases the energy barrier for phase transition which hinders water evaporation. Notably, the simulated reduction in the enthalpy of vaporization (h_{LV}) closely matches our experimental observations (Figure S17), thereby underscoring the importance of chaotropic chemistry to thermodynamically boosts water evaporation at the point-of-heating.

We further elucidate the mechanism behind the effects of chaotropic/kosmotropic chemistries on the water evaporation process by studying the energy-optimized molecular configurations of various surface-modified platforms and the water network. Comprehensive investigations unveil three important observations. (1) The surface molecules must interact with water molecule(s) via thiol-water intermolecular interactions, a key requisite to orientate neighboring water molecules and alter the water network. (2) Steric repulsion near a point-of-

attachment (e.g. the site of intermolecular interaction) between the thiol and water molecule hinders water-water interactions to disrupt the water hydrogen bonding network. Using MethoxyBT and MP thiols as an example, they are structurally similar except that the ArO-H in MP is replaced with a ArO-CH_3 group in MethoxyBT (Figure 3D-i). The bulkier methyl group in MethoxyBT sterically inhibits the bound water molecule from forming multiple hydrogen bonds with neighboring water molecules. This phenomenon reduces the extent of hydrogen bonding near the thermoplasmonic surface, thereby introducing disorderness to the neighboring water molecules and ultimately extending throughout the water network. The hypothesis is again affirmed by the faster water evaporation when using bulkier 1-mercapto-2-propanol (2.70 kg m^{-2} h^{-1} kW^{-1}) as the surface monolayer compared to linear 2-mercaptoethanol (2.46 kg m^{-2} h^{-1} kW^{-1}; Figure S18). Moreover, the thiol's aromatic backbone can also render steric repulsion to distort water molecular network when it contains a single-atom para-substituent (e.g., FTP and BTP) that interacts strongly with water (Figure S19). (3) For multidentate thiols with multiple points-of-attachment to water molecule(s), the separation distance between neighbouring electron donor/acceptor atoms can disruptively or constructively affect water-water interactions. For instance, both MBA and MPBA molecules have para-substituent comprising of multiple donors and/or acceptor atoms (Figure 3D-ii). For MBA, the O-donor and H-acceptor atoms are adjacent such that only one water molecule can interact with the carboxylic acid group via a two-point interaction. As a result, two out of the four hydrogen bonding sites on the bound H_2O molecule are blocked and cannot interact with nearby water molecules. This chemical effect weakens the water molecular network and promotes steam generation, similar to the case of MethoxyBT-plasmonic nanoheater. In contrast, the multiple O-donor and H-acceptor atoms in MPBA are more spaced out to allow concurrent interactions of thiol with two water molecules. The two chemically bound water molecules are in proximity which facilitates their water-water interactions and subsequent re-orientation to maximize intermolecular hydrogen bonding in the free water system. Such cooperative interaction between bound water molecules thus serves as a nucleation site to propagate water-water interactions for the formation of highly ordered water molecular network. This phenomenon consequently retards MPBA's steam generation because a larger energy input is required to overcome the strong and extensive hydrogen bonding network. Our finding thus highlights that disrupting the water hydrogen bonding network is critical to suppress the large energy barrier for enhanced water evaporation. These molecular-level insights also serve as vital rules-of-thumb for the precise design of chaotropic/kosmotropic functionalities to chemically boost/tune photothermal steam generation.

As a proof-of-concept application, we use the chaotropic-plasmonic nanoheater to purify contaminated water and further compare its performance with conventional Fenton-based chemical treatment, an important environmental catalysis for treating organic pollutants. We select methylene blue (MB) as a model organic pollutant because it is commonly found in aquatic environment with severe toxicity and poor intrinsic degradation rate.[33] In a typical setup, we perform photothermal-based water purification of MB-contaminated water samples (1mM; 13 mL) in a custom collection chamber by condensing the steam generated on the glass surfaces (Figure 4A). At pre-defined timings, we extract the water condensate and quantify the MB concentration present by correlating its absorption intensity at 665 nm with a standard calibration curve using UV-vis absorption spectroscopy (C_0 and C denote MB concentrations at 0 min and *t* min, respectively; Figure 4B, C; Figure S20, S21). Using the MethoxyBT-plasmonic nanoheater, the collected water exhibits negligible MB concentration and achieves a notable purification efficiency of 99.99 % (Figure 4D, E). In contrast, Fenton-based treatment of contaminated water demonstrates sluggish performance, attaining only ~17 % degradation efficiency after 30 min and ~38 % after 2 h even with the same initial pollutant concentration. It is noteworthy that a chemical treatment of 2 h provides a representative comparison because this duration is also required by our photothermal approach to purify 1 mL of the contaminated water. Our findings thus showcase the unprecedented use of chaotropic-plasmonic nanoheater to boost photothermal steam generation for the rapid purification of water at near-perfect efficiency, a feat that is otherwise challenging in traditional water treatment approaches. Moreover, the MethoxyBT-plasmonic nanoheater is easily reusable without needing intermediate treatment, as evident from the consistent water purification efficiencies of >99.99 % over 6 successive treatment cycles (Figure 4F).

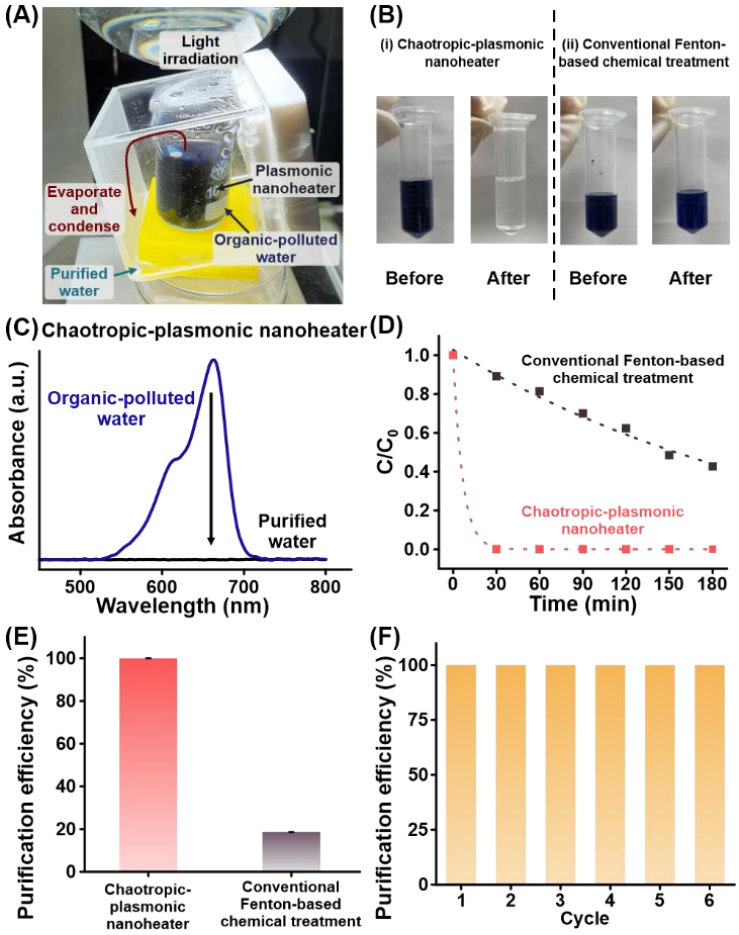

Figure 4. Application of chaotropic-plasmonic nanoheater for water purification. (A) Digital image showing a photothermal water purification set-up to treat organic-polluted water using light irradiation. (B) Photographs of water samples contaminated with methylene blue (MB) before and after treatment with (i) chaotropic MethoxyBT-plasmonic nanoheater or (ii) conventional Fenton-based chemical method. (C) UV-vis absorption spectra of contaminated water sample before and after photothermal water purification. (D) Time-dependent plots of normalized MB concentrations (C/C_0) and (E) the corresponding water purification efficiencies when using different water treatments. (F) Chaotropic-plasmonic nanoheater demonstrates consistent water purification efficiencies at ~100% over six repeated usage.

3. Conclusion

In conclusion, we have achieved efficient photothermal steam generation by incorporating functional molecular monolayers with unique chaotropic/kosmotropic chemistries onto thermoplasmonic material surfaces. Our chemical approach notably manipulates water-water interactions directly at the point-of-heating to alter/promote the water evaporation process. Comprehensive investigations into eight different surface chemistries reveal that the plasmonic nanoheater reaches the highest water evaporation rate (2.79 kg m^{-2} h^{-1} kW^{-1}) and a light-to-vapor conversion efficiency of ~83 % when using chaotropic MethoxyBT as the molecular monolayer. Notably, the chaotropic-plasmonic nanoheater evidently reduces the enthalpy of water vaporization by 1.6-fold when compared to bulk water, a phenomenon critical to generate more steam while using lesser energy input. Simulation studies highlight the superior photothermal steam generation in chaotropic-plasmonic nanoheater arises from its ability to disrupt water hydrogen bonding network which correspondingly suppresses the energy barrier for water evaporation. As a proof-of-concept application, our chaotropic-plasmonic design purifies organic-polluted water at near 100 % efficiency and excels over conventional chemical treatment. Our work on the unprecedented integration of chaotropic/kosmotropic chemistries with thermoplasmonic material thus offers a unique perspective to chemically boost steam generation beyond its photothermal property, with the aim to expedite our progress towards practical and decentralized water purification technologies. Moreover, these valuable insights can also be extended to other functional materials to achieve efficient water-related processes for diverse chemical, energy, and environmental applications, such as catalytic water splitting.

4. Experimental Section/Methods

Chemicals: Polyvinylpyrrolidone (MW = 1,300,000), hydroquinone (≥ 99 %), ethylene glycol (anhydrous, 99.8 %), silver nitrate (≥ 99 %), gold (III) chloride trihydrate (≥ 99.9 %), 4-methoxybenzenethiol (97 %), 4-mercaptobenzoic acid (99 %), 4-fluorothiophenol (98 %), 4-mercaptophenol (97 %), benzenethiol (97 %), 4-methylbenzenethiol (98 %), 4-mercaptophenylboronic acid (90 %), 4-bromothiophenol (95 %), 2-mercaptoethanol (≥ 99 %), 1-mercapto-2-propanol (95 %), Iron (II,III) oxide (97 %) and methylene blue were purchased from Sigma-Aldrich. Hydrogen peroxide (H_2O_2, 30%) was from Scharlab. Ethanol (≥ 99.8 %, absolute) was purchased from Thermo Fisher Scientific. Hydrochloric acid (37 %) was from Honeywell. Ammonia (ACS, Reag. Ph Eur) was from EMSURE. All chemicals were used without further purification. Milli-Q water (> 18.0 $M\Omega$. cm) was purified with a Sartorius Arium 611 ® UV ultrapure water system.

Synthesis and purification of silver chloride nanocubes: 0.4 g of PVP and 0.4 g of $AgNO_3$ were dissolved in 50 mL of cold ethylene glycol in sequence. 1 mL of 37 % hydrochloric acid was added dropwise into the mixture solution under stirring. The solution was then heated to 150 °C and kept stirring at 500 rpm for 20 minutes. After cooling down, 40 mL of acetone was added to 10 mL of resultant solution for sedimentation and centrifuged at 5000 rpm for 5 minutes. The obtained product was washed and dispersed in 10 mL of water to give a white suspension for further use.

Synthesis of nanoporous gold bowls (NPGBs): 0.554 mL of AgCl nanocube (7 mg mL^{-1}), 0.640 mL of hydroquinone solution (28 mM), and 0.400 mL of $HAuCl_4$ solution (40.372 mM) were sequentially added to 4.5 mL of PVP (MW = 1,300,000; 63 mM) solution with stirring at room temperature for 1 minute. The color of the reaction solution changed to dark grey. The AgCl/Au hybrid particles were centrifuged and washed with water. 2 mL of ammonia solution was added to remove the AgCl template. The colloidal solution was then centrifuged and washed with copious amount of water before being dispersed in 5 mL of ethanol.

Synthesis of solid gold bowls: 0.554 mL of AgCl nanocube (7 mg mL^{-1}), 0.640 mL of hydroquinone solution (28 mM), and 0.400 mL of $HAuCl_4$ solution (40.372 mM) were sequentially added to a vial with stirring at room temperature for 1 minute. The color of the reaction solution changed to dark grey. The AgCl/Au hybrid particles were centrifuged and

washed with water. 2 mL of ammonia solution was added to remove the AgCl template. The colloidal solution was then centrifuged and washed with copious amount of water before being dispersed in 5 mL of ethanol.

Fabrication of plasmonic nanoheater: The as-synthesized NPGBs in ethanol dispersion were dropcasted onto a round polyvinylidene fluoride (PVDF) membrane (pore size, 0.22 μm; diameter, 10 mm) via vacuum filtration. The membrane was then dried under ambient condition before further use.

Surface modification of plasmonic nanoheater: As-fabricated plasmonic nanoheater was immersed in 5 mL ethanolic thiol solution (5 mM) for 3 hours. The surface-modified plasmonic nanoheater was then washed with copious amount of ethanol and dried at ambient condition. SERS characterization was then employed to ensure successful NPGB surface modification by monitoring the vibrational fingerprint of various para-substituted thiolated arenes.

Evaluation of photothermal effect of plasmonic nanoheater (NPGB/PVDF film): The photothermal responses of various surface-modified plasmonic nanoheaters upon white LED light irradiation (100 W) were measured using an IR camera at pre-defined timing. Notably, white LED lamp was used for our photothermal and steam generation experiments because it is an energy-efficient light source which can be potentially coupled with renewable green electricity. Plasmonic nanoheater with a mass loading of 69 mg cm^{-2} was used to evaluate the photothermal conversion efficiency. All temperature measurements were repeated for at least 3 times to obtain the average value.

Evaluation of light-to-vapor conversion efficiency: The surface-modified plasmonic nanoheater with a mass loading density of 69 mg cm^{-2} was placed on top of water surface in a beaker containing 13 mL water. The diameter of the water surface area was estimated to be ~4.1 cm^2. Upon light irradiation, the time-dependent changes of water mass were recorded using an analytical balance to determine the water evaporation rate and the associated light-to-vapor conversion efficiency.

Density functional theory (DFT) simulations: The calculation on the interaction of thiol-modified Au surface with water molecules was conducted using unrestricted B3LYP exchange-

correlation functional, as implemented in the Gaussian 09 computational chemistry package. The 6-31G (d,p) basis set was used for all atoms except Au, for which the LANL2DZ basis set was employed. The Au surface was modeled using a reported model consisting of 5 Au atoms. After geometry optimization of the Au5 cluster, the thiol was then covalently bonded to the Au cluster and the entire system was re-optimized with the Au atoms fixed. Water molecule (1 – 5 molecules) was subsequently placed near the Au-thiol system to study their molecular-level interactions on an atomic level.

Quantification of methylene blue (MB) in the purified water: A calibration curve relating absorption intensity with MB concentration was first established for subsequent quantification in the solution. MB was first dissolved in ultrapure water and further serial-diluted to various concentration between 1×10^{-7} M and 5×10^{-5} M. The absorption spectra were obtained using UV-vis absorption spectroscopy and further used for quantification using the characteristic peak at 665 nm.

Contaminated water purification: 13 mL of water contaminated with methylene blue (1 mM) was added into a beaker. A MethoxyBT-plasmonic nanoheater was then placed on top of the contaminated water and the entire set-up was positioned in a customized vapor condensation system. Upon light irradiation, photothermal steam generation occurred and the condensate was collected on the quartz cell. The clean water produced was then transferred into a cuvette for further characterization using UV-vis absorption spectroscopy.

Conventional Fenton-based chemical treatment of contaminated water: 0.1 mL of water contaminated with methylene blue (10 mM) was added into a 2 mL micro-centrifuge tube, followed by 0.9 mL of H_2O_2 solution (30% v/v). 35 mg of commercially available Fe_3O_4 was added into the reaction solution. A 100 µL aliquot of the reaction solution was extracted at pre-defined interval of 30 min for a total experimental duration of 180 min. The aliquot collected was then transferred into a cuvette for subsequent characterization using UV-visible spectroscopy.

Characterization: Scanning electron microscopy (SEM) images were collected on a JEOL-JSM-7600F microscope operated at 5kV. Contact angles were measured on a Theta Lite tensiometer equipped with a Firewire digital camera. Static contact angles were measured with a 5 µL ultrapure water droplet. SERS measurements were performed using x-y and x-z

hyperspectral imaging mode of the Ramantouch microspectrometer (Nanophoton Inc, Osaka, Japan) at an excitation wavelength of 532 nm. A 20× (N.A. 0.45) objective lens with 10 s acquisition time was used for data collection with Raman shift ranging from 400 to 1800 cm^{-1}. IR thermal imaging camera (UNI-T, model: UTi260B) was used to capture the temperature of NPGB/PVDF film. XPS spectra were measured using a Phoibos 100 spectrometer with a monochromatic Mg X-ray radiation source. Diffuse reflectance measurement was conducted with an AvaSpec-ULS2048CL-EVO-UA-50 and an integrating sphere containing a halogen light source (AvaSphere-50-LS-HAL-12V). UV-vis spectroscopic measurements were conducted using an AvaSpec-ULS2048CL-EVO-UA-50 equipped with a deuterium-halogen light source (AvaLight-DH-S).

Supporting Information

Supporting Information is available from the Wiley Online Library or from the author.

Acknowledgements

H.K.L. thanks the funding supports from Singapore Ministry of Education (AcRF Tier 1 RS13/20 and RG4/21), A*STAR Singapore (AME YIRG A2084c0158), National University of Singapore Center of Hydrogen Innovation (CHI-P2022-05), and Nanyang Technological University start-up grants. The research was conducted as a part of NICES (NTU-IMRE Chemistry Lab for Eco Sustainability; REQ0275931), a joint research initiative between Nanyang Technological University (NTU) and Institute of Materials Research and Engineering (IMRE) from Agency for Science, Technology and Research (A*STAR). C.C. and Z. N. T. contributed equally to this work.

Received: ((will be filled in by the editorial staff))
Revised: ((will be filled in by the editorial staff))
Published online: ((will be filled in by the editorial staff))

References

(1) G. Di Baldassarre, M. Sivapalan, M. Rusca, C. Cudennec, M. Garcia, H. Kreibich, M. Konar, E. Mondino, J. Mård, S. Pande, M. R. Sanderson, F. Tian, A. Viglione, J. Wei, Y. Wei, D. J. Yu, V. Srinivasan, G. Blöschl *Water Resour. Res.* **2019,** *55,* 6327.
(2) N. Y. Donkadokula, A. K. Kola, I. Naz, D. Saroj *Rev. Environ. Sci. Biotechnol.* **2020,** *19,* 543.
(3) V. Albergamo, B. Blankert, E. R. Cornelissen, B. Hofs, W.-J. Knibbe, W. van der Meer, P. de Voogt *Water Res.* **2019,** *148,* 535.
(4) Y. Lin, H. Xu, X. Shan, Y. Di, A. Zhao, Y. Hu, Z. Gan *J. Mater. Chem. A* **2019,** *7,* 19203.
(5) M. Gao, L. Zhu, C. K. Peh, G. W. Ho *Energy Environ. Sci.* **2019,** *12,* 841.
(6) P. Tao, G. Ni, C. Song, W. Shang, J. Wu, J. Zhu, G. Chen, T. Deng *Nature Energy* **2018,** *3,* 1031.
(7) I. Ibrahim, D. H. Seo, A. M. McDonagh, H. K. Shon, L. Tijing *Desalination* **2021,** *500,* 114853.
(8) B. Cieślik, P. Konieczka *J. Clean. Prod.* **2017,** *142,* 1728.
(9) Z. Zhang, Y. Chen *Chem. Eng. J.* **2020,** *382,* 122955.
(10) A. Politano, P. Argurio, G. Di Profio, V. Sanna, A. Cupolillo, S. Chakraborty, H. A. Arafat, E. Curcio *Adv. Mater.* **2017,** *29,* 1603504.
(11) P. Zhang, J. Li, L. Lv, Y. Zhao, L. Qu *ACS Nano* **2017,** *11,* 5087.
(12) D. Shin, G. Kang, P. Gupta, S. Behera, H. Lee, A. M. Urbas, W. Park, K. Kim *Adv. Opt. Mater.* **2018,** *6,* 1800317.
(13) Y. Jin, J. Chang, Y. Shi, L. Shi, S. Hong, P. Wang *J. Mater. Chem. A* **2018,** *6,* 7942.
(14) Z. Xie, Y. Duo, Z. Lin, T. Fan, C. Xing, L. Yu, R. Wang, M. Qiu, Y. Zhang, Y. Zhao, X. Yan, H. Zhang *Adv. Sci.* **2020,** *7,* 1902236.
(15) K.-K. Liu, Q. Jiang, S. Tadepalli, R. Raliya, P. Biswas, R. R. Naik, S. Singamaneni *ACS Appl. Mater. Interfaces* **2017,** *9,* 7675.
(16) D. P. Storer, J. L. Phelps, X. Wu, G. Owens, N. I. Khan, H. Xu *ACS Appl. Mater. Interfaces* **2020,** *12,* 15279.
(17) X. Han, L. V. Besteiro, C. S. L. Koh, H. K. Lee, I. Y. Phang, G. C. Phan-Quang, J. Y. Ng, H. Y. F. Sim, C. L. Lay, A. Govorov, X. Y. Ling *Adv. Funct. Mater.* **2021,** *31,* 2008904.
(18) Z. Yang, X. Han, H. K. Lee, G. C. Phan-Quang, C. S. L. Koh, C. L. Lay, Y. H. Lee, Y.-E. Miao, T. Liu, I. Y. Phang, X. Y. Ling *Nanoscale* **2018,** *10,* 16005.
(19) S. Yu, Y. Zhang, H. Duan, Y. Liu, X. Quan, P. Tao, W. Shang, J. Wu, C. Song, T. Deng *Sci. Rep.* **2015,** *5,* 13600.
(20) H. Chen, L. Shao, T. Ming, Z. Sun, C. Zhao, B. Yang, J. Wang *Small* **2010,** *6,* 2272.
(21) J. D. Smith, C. D. Cappa, K. R. Wilson, B. M. Messer, R. C. Cohen, R. J. Saykally *Science* **2004,** *306,* 851.
(22) K. I. Assaf, W. M. Nau *Angew. Chem. Int. Ed.* **2018,** *57,* 13968.
(23) Z. Zhang, X. Wu, L. Wang, B. Zhao, J. Li, H. Zhang *RSC Advances* **2017,** *7,* 13451.
(24) E. Pensa, E. Cortés, G. Corthey, P. Carro, C. Vericat, M. H. Fonticelli, G. Benítez, A. A. Rubert, R. C. Salvarezza *Acc. Chem. Res.* **2012,** *45,* 1183.
(25) M. Chen, I. Y. Phang, M. R. Lee, J. K. W. Yang, X. Y. Ling *Langmuir* **2013,** *29,* 7061.
(26) Y. Yang, R. Zhao, T. Zhang, K. Zhao, P. Xiao, Y. Ma, P. M. Ajayan, G. Shi, Y. Chen *ACS Nano* **2018,** *12,* 829.
(27) J. Yang, Y. Pang, W. Huang, S. K. Shaw, J. Schiffbauer, M. A. Pillers, X. Mu, S. Luo, T. Zhang, Y. Huang, G. Li, S. Ptasinska, M. Lieberman, T. Luo *ACS Nano* **2017,** *11,* 5510.
(28) K. Bae, G. Kang, S. K. Cho, W. Park, K. Kim, W. J. Padilla *Nat Commun* **2015,** *6,* 10103.
(29) X. Li, W. Xu, M. Tang, L. Zhou, B. Zhu, S. Zhu, J. Zhu *Proc. Natl. Acad. Sci. U. S. A.* **2016,** *113,* 13953.
(30) X. Hu, W. Xu, L. Zhou, Y. Tan, Y. Wang, S. Zhu, J. Zhu *Adv. Mater.* **2017,** *29,* 1604031.

(31) Q. Ma, P. Yin, M. Zhao, Z. Luo, Y. Huang, Q. He, Y. Yu, Z. Liu, Z. Hu, B. Chen, H. Zhang *Adv. Mater.* **2019,** *31,* 1808249.
(32) Y. Guo, X. Zhou, F. Zhao, J. Bae, B. Rosenberger, G. Yu *ACS Nano* **2019,** *13,* 7913.
(33) X.-S. Hu, R. Liang, G. Sun *J. Mater. Chem. A* **2018,** *6,* 17612.